

Vertical stacking of three-dimensional nanostructures via an aerosol lithography for advanced optical applications

Kiwoong Lee¹, Hoseop Choi², Dae Seong Kim¹, Min Seok Jang^{3,5}  and Mansoo Choi^{1,4,5}

¹ Global Frontier Center for Multiscale Energy Systems, Seoul National University, Seoul 08826, Republic of Korea

² Samsung Electronics Mechatronic R&D Center, Hwaseong 18848, Republic of Korea

³ School of Electrical Engineering, Korea Advanced Institute of Science and Technology, Daejeon 34141, Republic of Korea

⁴ Department of Mechanical and Aerospace Engineering, Seoul National University, Seoul 08826, Republic of Korea

E-mail: jang.minseok@kaist.ac.kr and mchoi@snu.ac.kr

Received 12 July 2017, revised 25 September 2017

Accepted for publication 27 September 2017

Published 31 October 2017



CrossMark

Abstract

In this report, we introduce a method utilizing ion-assisted aerosol lithography to stack 3D nanostructures vertically. The stacked 3D nanostructures exhibit extraordinary optical properties: the double layer 3D nanostructures show more than 5-fold increased surface enhanced Raman scattering intensities compared to their single layer counterpart. This unusual enhancement of Raman intensity implies the existence of additional vertical hotspots formed by interlayer cavity effects between the lower and upper nanostructures. Allowing for full three-dimensional control in nanofabrication, this work provides a reliable way to create complex-shaped advanced optical nanostructures with non-intuitive bulk optical properties.

Supplementary material for this article is available [online](#)

Keywords: aerosol, spark discharge, nanostructure, electromagnetic hotspot, surface enhanced Raman spectroscopy (SERS)

(Some figures may appear in colour only in the online journal)

1. Introduction

Three-dimensional (3D) nanostructures have attracted tremendous interest due to their wide applicability in various fields of research [1–16]. Their high surface-to-volume ratio and complicated geometries with vertical variations are especially useful in designing advanced nanophotonic applications, including 3D metamaterials [1–4], high efficiency energy devices such as fuel cells [5, 6] and photovoltaics [7–12]. Also, their inherent advantages enable to be exploited in a biomedical applications, such as bioassay [13, 14]. In order to fabricate 3D nanostructures with various geometries,

diverse techniques have been studied. One way to create 3D nanostructures is stacking 2D planar nanostructures in a vertical direction through successive lithography and etching steps [1, 2, 4, 15]. This method is considered as the easiest way to fabricate 3D nanostructures when the geometry is simple, but it requires too many lithographic steps when the geometry has complicated vertical variation. On the other hand, more elaborate methods such as electron beam lithography [16], focused ion-beam milling [17, 18] or two-photon absorption lithography [19, 20] allow for fabricating 3D nanostructures with more complex geometries. However, these techniques are difficult to be adopted for large scale mass production, since these methods require focused light or beam to be scanned serially along every voxel of the 3D

⁵ Authors to whom any correspondence should be addressed.

nanostructures. Additionally, these methods require expensive installation.

Ion-assisted aerosol lithography (IAAL) operating at atmospheric conditions provides a reliable way to create 3D nanostructures without the limitations of the conventional methods. Our group recently demonstrated that the periodic arrays of various shaped 3D nanostructures can be constructed in a uniform and reproducible way through IAAL [21–24], and the 3D nanostructures via IAAL can be applied to photovoltaic devices [10, 11]. Also, It was shown that these nanostructures have electromagnetic hotspots to substantially increase surface-enhanced Raman spectroscopy (SERS) signal for single molecule detection [25]. However, it should be pointed out that the nanostructures fabricated through the previous IAAL method are still quasi-3D; Although their lateral shape can be freely controlled by modulating the substrate pattern, the flow rate of charged aerosols, and the electrostatic potential applied to the substrate, the control on their vertical variation is limited. Herein, in order to obtain full 3D control on the shapes of aerosol-assembled nanostructures, we developed a vertical stacking method for IAAL. We fabricated a bi-layer 3D flower-shaped nanostructures through repetitive executions of IAAL nanoparticle assembly.

SERS is employed in detecting and identifying small amount of single molecules since it significantly magnifies the Raman scattering intensity of molecules adsorbed onto metal surface. Owing to its high sensitivity, there have been intense efforts to utilize SERS technology in various fields, such as chemical [26] and biological [27] detection and cell visualization and drug delivery [28]. Our group previously demonstrated that flower-shape 3D nanostructures fabricated through IAAL exhibit excellent optical performance as a SERS substrate. In this work, we demonstrates that the optical performance of 3D nanostructures can be further improved by stacking them in vertical direction via repetitive execution of IAAL. The optimized bi-layer 3D nanostructure exhibited about 5.4 times increased SERS signal compared to the mono-layer 3D structure. By rigorous full wave electromagnetic simulations, we revealed that this abnormal enhancement in SERS signal originates from additional electromagnetic hotspots formed between the layers.

2. Experimental details

2.1. Fabrication of bi-layer 3D nanostructures via IAAL

As illustrated in figure S1(a), which is available online at stacks.iop.org/NANO/28/475302/mmedia, our IAAL nanofabrication device is composed of three chambers: a corona chamber that generates nitrogen cations; a spark discharge chamber that generates charged Cu nanoparticles; and a deposition chamber where Cu nanoparticles are assembled to form 3D nanostructures. Nitrogen cations are first generated at the positively biased (3.2 kV) tungsten tip in the corona chamber, and blown for 30 min to the deposition chamber where a patterned resist on Si substrate is installed. We adopted heavily doped (boron) and thus conductive Si

substrate with resistivity of 1.0–30.0 Ω cm and orientation of $\langle 111 \rangle$. It is well known that a few hundreds nanometer scale resist patterning can be done by photolithography, however, in this study, the patterning step was performed by electron-beam lithography owing to the availability. The Si substrate is negatively biased (–6 kV) and thus attracts the nitrogen cations. As the nitrogen cations are deposited on the patterned substrate, positive charges are built up on the area covered by insulating resist layer, whereas the exposed conductive Si remains neutral. This selective accumulation of the positive charges creates electrostatic lenses to focus the electric fields onto the exposed conductive area. Positively charged Cu nanoparticles generated by spark discharge from the positively biased (5.0 kV) Cu pin to the grounded Cu plate are blown into the deposition chamber by nitrogen carrier gas with the flow rate of 4 lpm. This pin-to-plate type spark discharge method is advantageous in generating unagglomerated nanoparticles with narrow size distribution [29]. Throughout the experiment, we measured particle size distribution of the Cu nanoparticles by using scanning mobility particle sizer system (Differential Mobility Analyzer 3085 and Condensation Particle Counter 3776, TSI). The average diameter and the volume concentration of generated nanoparticles were maintained as 4 nm and $2 \times 10^8 \text{ nm}^3 \text{ cm}^{-3}$ (figure S2), respectively. Due to the electrostatic lensing effect by accumulated positive charges resist, the positively charged Cu nanoparticles are attracted to the exposed Si region, where a negative bias voltage of –3.5 kV is applied. These nanoparticles are assembled in a converging manner and start forming vertical nanostructures. As the nanostructures become taller than the e-beam resist layer, they start growing both in lateral and vertical directions due to the repelling electric field of the selectively accumulated positive charges.

The shape of 3D nanostructures created via IAAL strongly depends on the shape of the patterns etched on the resist, because it determines the electrostatic potential landscape after the nitrogen cation deposition process. Here, we patterned square arrays of 1.5 μm long cross shapes with a 3 μm period (figure S1(b)) on 100 nm thick resist (Zep520a, Zeon) as shown in figure 1(a) via standard electron beam lithography (JBX9300FS, JEOL). The four-fold symmetry imposed by the resist pattern forces nanostructures to branch out in four different directions and to consequently form 3D flower shape with four petals as depicted in figure 1(b). The total area of the pattern was 200 μm by 200 μm in this experiment, but can be extended to centimeter or larger scale by using multi-pin spark discharge [30]. After creating the first layer of 3D nanostructures, we sintered the nanostructures through electron beam irradiation (figure 1(c)), because the assembled 3D nanostructures are too porous and fragile to endure the successive fabrication processes for constructing the next stacking layer of 3D nanostructures. The electron beam was accelerated by 10 kV and irradiated for 12 min.

The procedures to vertically stack an additional layer of 3D nanostructures on top of the existing nanostructures are summarized in figures 1(d)–(g). We spin-coated the second resist layer of resist such that the top surface of the layer was

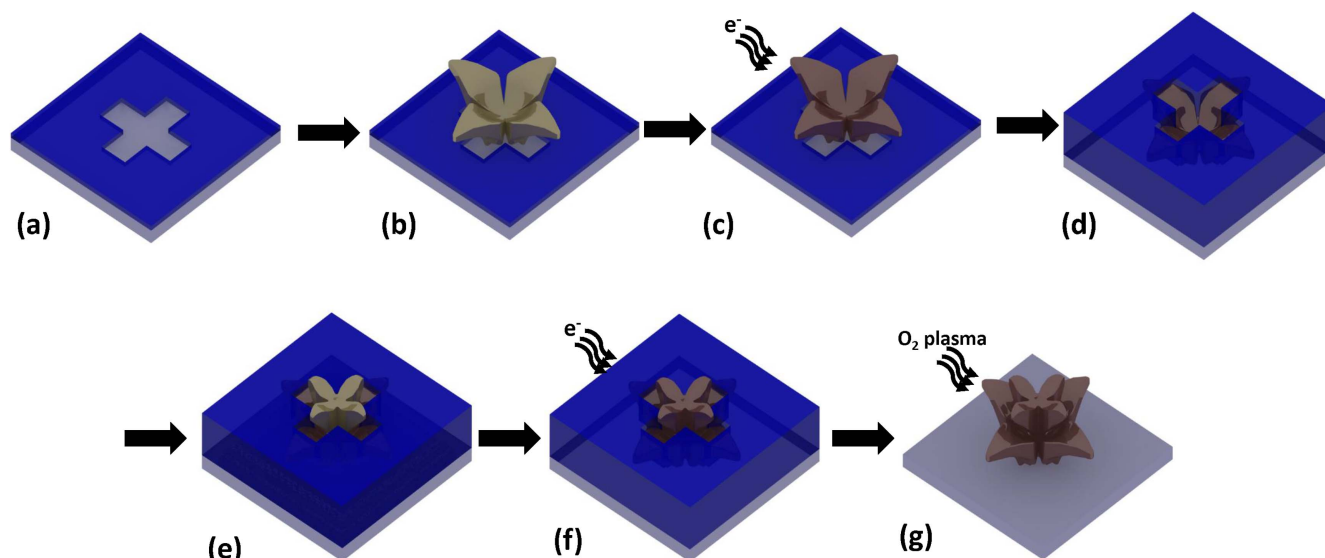


Figure 1. Schematics of stacking 3D nanostructures. (a) Preparation of resist patterns. (b) Fabrication of 3D nanostructures via IAAL. (c) Sintering nanostructures via electron beam irradiation. (d) Preparation of another patterns for the upper nanostructures after spin-coating the resist. (e) Fabrication of the upper nanostructures. (f) Sintering nanostructures. (g) Removal of the resist.

100 nm above the surface of the existing 3D nanostructures, and patterned the periodic square shapes (figure 1(d)). The alignment between the first and the second layers was adjusted by using alignment keys that were pre-patterned on the silicon substrate via photolithography. Using the second layer of the resist patterns, additional 3D nanostructures were then fabricated via IAAL under the same conditions under which the first layer was grown (figure 1(e)). Here again, the selective charge accumulation on the area covered by the resist causes electrostatic lensing effect, which allows for depositing the second layer of nanostructures right on top of the surface of the existing 3D nanostructures. The newly formed 3D nanostructures were then reinforced by e-beam sintering as illustrated in figure 1(f). Finally, the residual e-beam resist was eradicated through O₂ plasma ashing as illustrated in figure 1(g), with the plasma power of 300 W, the frequency of 2.45 GHz and the gas flow of 300 sccm for 15 min (V15-G, Plasma Finish).

2.2. SERS measurement of 3D nanostructures

To demonstrate enhanced photonic performance of bi-layer 3D nanostructures over mono-layer 3D nanostructures, we measured and compared the surface-enhanced Raman scattering (SERS) of thiophenol (C₆H₆S) molecules chemisorbed onto the surface of both the mono- and bi-layer 3D nanostructures. To facilitate adsorption of thiophenol molecules onto the surface of the 3D nanostructures, we conformally coated our 3D nanostructures with a 5 nm chromium adhesive layer and a 50 nm thick gold layer using tilting thermal evaporator. By dipping the gold-coated nanostructures into 1×10^{-4} M ethanolic solution of thiophenol for 12 h, thiophenol molecules were then chemisorbed onto the surface of the 3D nanostructures. For the measurement of Raman spectra, we illuminated the samples with a He-Ne laser with a beam spot size of 850 nm (100x objective with NA = 0.9),

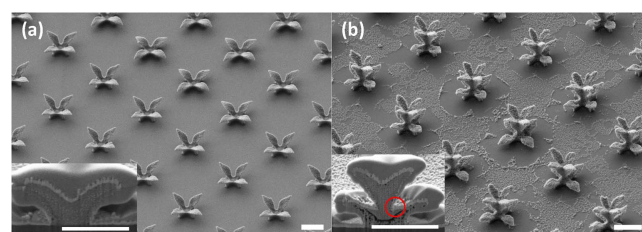


Figure 2. SEM images of (a) mono-layer 3D nanostructures and (b) bi-layer 3D nanostructures. The scale bar represents 1 μ m in length.

irradiation power of 0.16 mW, and the wavelength of 633 nm, and measured the intensity of inelastically scattered light using a LN₂ cooled CCD detector (LabRam HR, Horiba Jobin-Yvon) for 30 s. The measurement was conducted for the five different spots of each sample in order to identify photonic uniformity of the sample.

3. Results and discussion

3.1. Fabrication of bi-layer 3D nanostructures

Figure 2 presents the field-emission scanning electron microscopy images of the resulting mono-layer and bi-layer 3D nanostructures. For these samples, both the upper and the lower 3D nanostructures were deposited for 30 min, but the upper ones turned out to be smaller (~1100 nm wide) than the lower ones (~1800 nm), because in the early stage of upper nanostructure deposition, the injected nanoparticles are used to fill up the concave surface of the lower nanostructures.

To fully understand the electrostatically driven particle deposition process, we also carried out numerical simulations for the trajectories of nanoparticles under the electric potential distributions formed by accumulated charges on the e-beam resist and assembled nanoparticles [31]. Here, the interaction

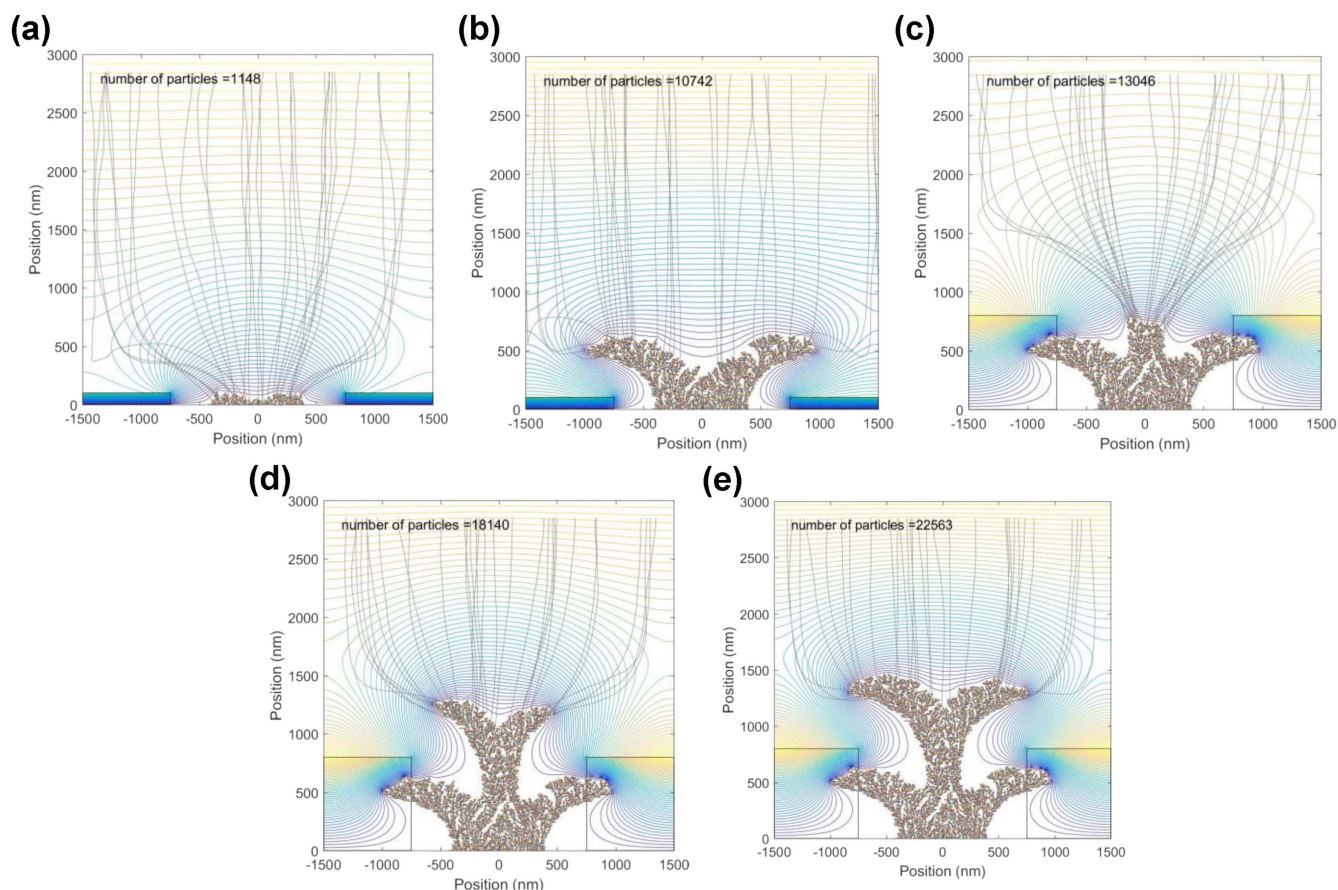


Figure 3. Numerical calculation results for the particle trajectories and deposition under electric potential distributions formed by accumulated charges on the e-beam resist and assembled nanoparticles. (a) Initial growth stage. (b) Formation of mono-layer 3D nanostructure. (c) Initial growth stage of upper 3D nanostructure after additional e-beam lithography. (d), (e) Lateral growth of upper 3D nanostructure.

among injected charged particles is ignored during their flight, and the deposited Cu particles are assumed to be perfect conductors so that they possess the same electric potential as the substrate. The accumulated surface charge in the numerical simulations is set to $3.63 \times 10^{-4} \text{ C m}^{-2}$, which is adopted from our previous measurements using Kelvin force microscope [23]. Figure 3 shows the snapshots of the calculated particle trajectories at various stages of the deposition process. Even though the numerical calculation was two-dimensional, the result captures the essential physics of IAAL and well mimics the cross-section of the real structures, as inferred from the comparison between figure 3(e) and the inset of figure 2(b). From these simulations, it is clear that the electrostatic focusing still works even on the curved top surface of the first layer nanostructures, which assures the growth of the second layer 3D nanostructures.

3.2. SERS of bi-layer 3D nanostructures

The measured Raman spectra of thiophenol molecules chemisorbed onto the 4-petals mono- and bi-layer nanostructures (figures 2(a) and (b)) are shown in figure 4 and table S1. Both spectra exhibit four distinctive Raman peaks of thiophenol at 997, 1023, 1075, and 1575 cm^{-1} , which correspond to CCC ring in-plane bending mode, CH in-plane bending mode,

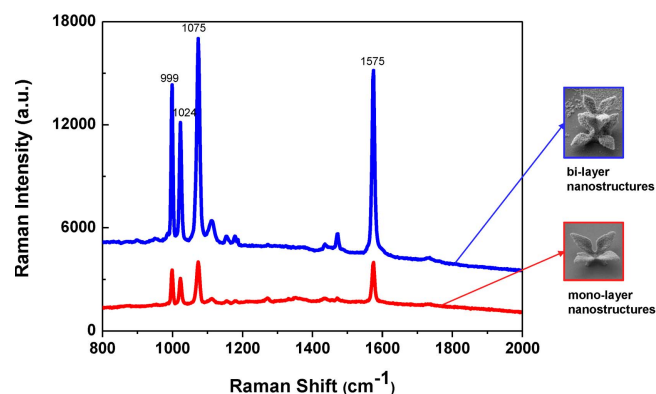


Figure 4. Raman spectra of mono-layer 3D nanostructure and bi-layer 3D nanostructure.

in-plane CCC ring breathing mode with CS stretching mode, and CC stretching mode, respectively [32]. The intensities of Raman peaks are consistently much higher for the bi-layer 3D nanostructures than for the mono-layer nanostructures. The relative enhancement factors of the bi-layer 3D nanostructures comparing to the mono-layer 3D nanostructures are 4.51, 4.51, 4.74, and 4.58 for the peaks at 997 cm^{-1} , 1023 cm^{-1} , 1075 cm^{-1} , and 1575 cm^{-1} , respectively. Also, we measured SERS signals of additional identical samples for the

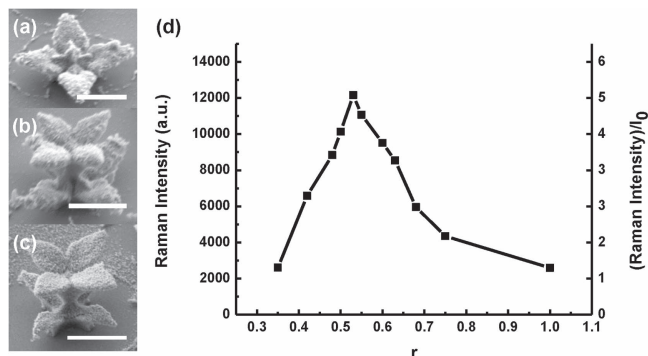


Figure 5. Size variation of upper 3D nanostructure. (a) Upper nanostructures is much smaller than lower nanostructures. (b) Upper nanostructure is half of the lower nanostructure in size. (c) Upper nanostructure is equal to lower nanostructure in size. (d) Peak intensity of the bi-layer 3D nanostructures according to the size of the upper nanostructures. The value of r and I_0 represent the ratio of the size of the upper nanostructures to the size of the lower nanostructures and the peak intensity of the mono-layer 3D nanostructures.

mono-layer and the bi-layer nanostructures to confirm the reproducibility of our fabricating techniques and SERS behavior (see table S1).

To further investigate the effect of the upper 3D nanostructures on SERS enhancement, we varied the size of upper 3D nanostructures while maintaining the lower 3D nanostructures as wide as 1800 nm. The lateral size of the upper 3D nanostructures was determined by the deposition time of the charged Cu nanoparticle during IAAL. We varied the deposition time from 10 min to 1.5 h to obtain the upper 3D nanostructures with lateral size from 400 to 1700 nm. Figure 5(d) shows how the relative size of the upper 3D nanostructure (r) affects the SERS intensity of the bi-layer 3D nanostructures at Raman shift of 1575 cm^{-1} . The measurement was conducted for five different spots of each sample (table S2) and the average values are represented in figure 5(d) and figure S3. Here, r is defined as the lateral size ratio of the upper 3D nanostructures to the lower 3D nanostructures, and the SERS intensity of the bi-layer nanostructures is normalized by that of the mono-layer nanostructures (I_0). The measured SERS enhancement ratio (I/I_0) has a maximum of 5.41 at around $r = 0.5$, and rapidly decreases and approaches to unity (no enhancement) as r deviates from 0.5. This trend can be explained by a combination of two effects: On the one hand, when the nanoparticle deposition time is short, the upper 3D nanostructures are not fully grown and their shape looks more like a dull pillar rather than a flower with distinctive four petals as shown in figure 5(a). Consequently, smaller nanostructures have less sharp edges and corners, and thus possess weaker electromagnetic hotspots for SERS enhancement compared to fully grown nanostructures; on the other hand, as the second layer nanostructures become larger, they screen significant portion of the first layer nanostructures under illumination, diminishes the overall SERS enhancement. Once r becomes unity or larger as shown in figure 5(c), the first layer is almost completely shaded by the second layer and thus the SERS

intensity of the bi-layer nanostructure becomes equal to I_0 . For the optimal size of $r = 0.5$, every hotspot of the 3D nanostructures of the both layers is most efficiently exposed to the incident light.

Also, it is noteworthy that even though the number of thiophenol molecule illuminated by incident light is increased less than twice by stacking an additional layer of 3D nanostructures, SERS peak intensities are increased more than twice. Another interesting point is that, for the optimized bi-layer structure, the SERS intensity was enhanced by more than fivefold, while the total number of petals was simply doubled by stacking two 3D nanostructures with the same number of the petals. In order to reveal the origin of this abnormal enhancement, we performed full-wave electromagnetic simulations using the finite difference time domain method (Lumerical FDTD simulation software). Figure 6(b) shows the simulated electric field intensity profile of horizontal cross-sections of the bi-layer 3D nanostructures with $r = 0.5$. As reported in the previous work [25], the electromagnetic hotspots are formed at the gaps between adjacent petals of both upper and lower 3D nanostructures as shown in the cross-section $A-A'$ and $C-C'$. More interestingly, as illustrated in the cross-section $B-B'$, we found that the electric field is also enhanced in the vicinity of the pillar connecting upper and lower 3D nanostructures. The vertical cross-section for $r = 0.5$ shown in the middle panel of figure 6(c) clearly reveals that there exist additional hotspots at the vertical nanogaps between the upper and the lower nanostructures, causing the abnormal SERS enhancement. Here, the top surface of the upper 3D nanostructure and the bottom surface of the lower nanostructure cause multiple reflections of the incident light, effectively forming an optical cavity to magnify the intensity of the electric field. Note that, however, this interlayer optical cavity effect becomes much weaker when the upper 3D nanostructures are too small or too large as shown in figure 6(c). For small r , the petals, which serve as the upper mirror plates for the interlayer cavities, are not fully grown and thus cannot effectively confine light, whereas for large r , the incident light is mostly screened by the upper 3D nanostructure and hardly reaches the top surface of the lower 3D nanostructure.

It was demonstrated that the array of mono-layer 3D nanostructures with 4-fold flower shape can be used as SERS substrate with sufficient enhancement factor for detecting single molecule, by Jung *et al* [25]. Therefore, in the case of the array of bi-layer 3D nanostructures, it can be also used as SERS substrate with improved enhancement factor since bi-layer 3D nanostructures exhibit increased SERS signal intensity more than fivefold while the number of thiophenol molecules adsorbed onto the surface of the nanostructures is increased less than twice.

4. Conclusions

We demonstrated vertical stacking of 3D nanostructures by repetitive execution of 3D assembly of charged aerosols via IAAL. The resulting bi-layer 3D flower-shaped nanostructures

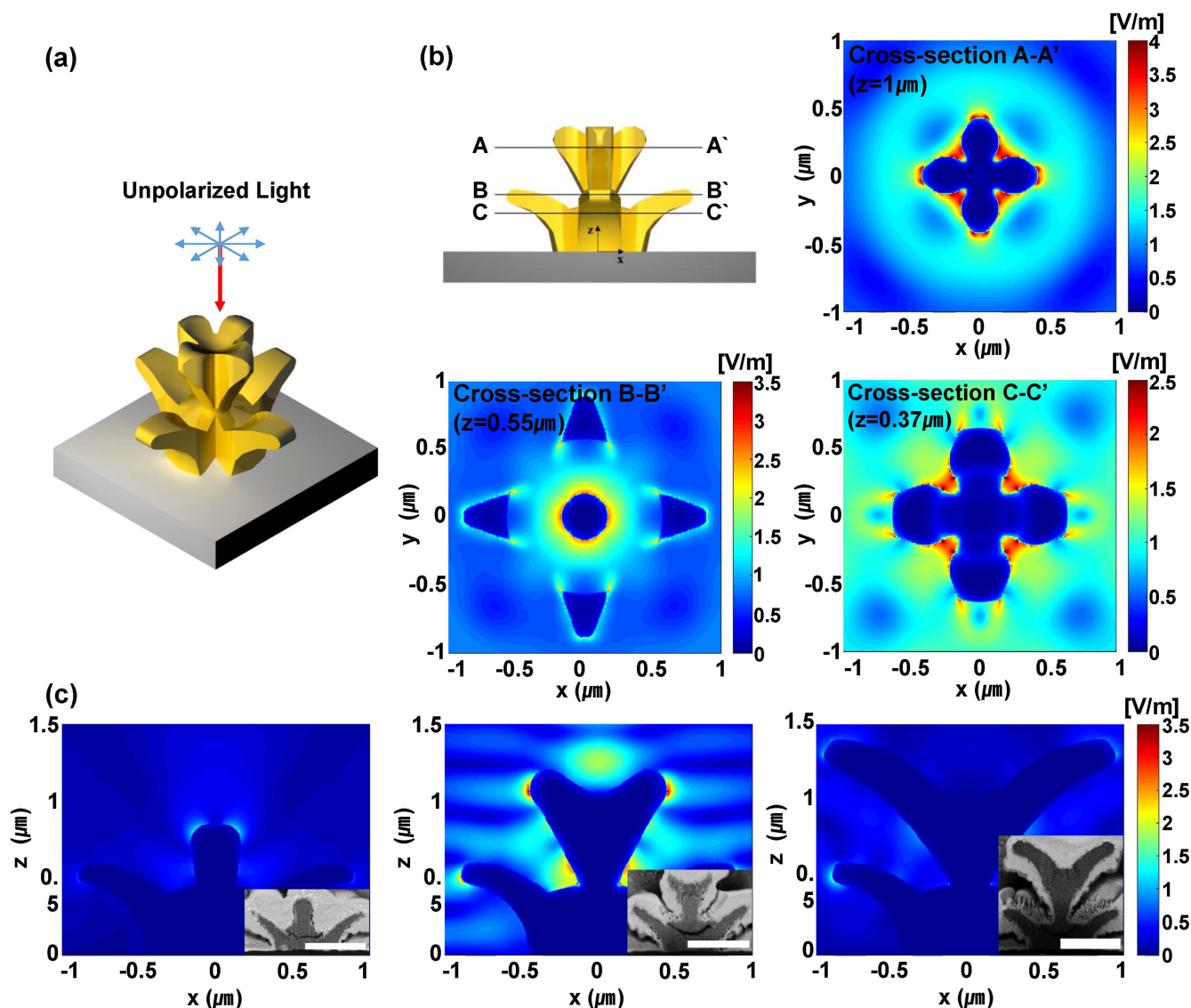


Figure 6. Electromagnetic simulations for the bi-layer nanostructures. (a) Schematic view of the simulation model. Even though the substrates are coated with gold as same as the nanostructures, the color of the substrates and nanostructures are illustrated dissimilarly for the visibility (b) electric field intensity distribution of horizontal cross-section of the bi-layer 3D nanostructure. It can be identified that every hotspot of upper and lower 3D nanostructure and vertical hotspots strongly interacts with incident light. (c) Electric field intensity distribution of vertical cross-section. Each figure is represented in the same color scale as represented in the color bar on the right. Each inset represents SEM images for the cross section of each nanostructure and every scale bar represents $1 \mu\text{m}$. In the case that the upper nanostructure is the half of the lower nanostructure in size, the gaps between vertically adjacent petals play a role as hotspots.

exhibit more than fivefold enhanced SERS intensity compared to the monolayer flower-shaped 3D nanostructures. From full-wave optical simulations on these structures, we found that this anomalous enhancement in optical performance originates from the formation of additional electromagnetic hotspots at the vertical nanogaps between the upper and the lower nanostructures. This vertical stacking technique can be readily generalized to produce multi-layer 3D nanostructures. Moreover, by using different lithographic patterns for each layer growth, 3D nanostructures with various geometries can be stacked on top of each other, providing an additional degree of freedom in designing advanced 3D photonic nanostructures such as bulk metamaterials.

Acknowledgments

This work was supported by the Global Frontier R&D Program on Center for Multiscale Energy System (Grant no.2012M3A6A7054855) and by the Creative Materials Discovery Program (Grant no.2016M3D1A1900038, M S Jang) through the National Research Foundation of Korea (NRF) funded by the Ministry of Science, ICT and Future Planning.

ORCID iDs

Min Seok Jang  <https://orcid.org/0000-0002-5683-1925>

References

- [1] Lin S-Y, Fleming J, Hetherington D, Smith B, Biswas R, Ho K, Sigalas M, Zubrzycki W, Kurtz S and Bur J 1998 A three-dimensional photonic crystal operating at infrared wavelengths *Nature* **394** 251–3
- [2] Liu N, Guo H, Fu L, Kaiser S, Schweizer H and Giessen H 2008 Three-dimensional photonic metamaterials at optical frequencies *Nat. Mater.* **7** 31–7
- [3] Gansel J K, Thiel M, Rill M S, Decker M, Bade K, Saile V, von Freymann G, Linden S and Wegener M 2009 Gold helix photonic metamaterial as broadband circular polarizer *Science* **325** 1513–5
- [4] Helgert C, Pshenay-Severin E, Falkner M, Menzel C, Rockstuhl C, Kley E-B, Tünnermann A, Lederer F and Pertsch T 2011 Chiral metamaterial composed of three-dimensional plasmonic nanostructures *Nano Lett.* **11** 4400–4
- [5] Sun S, Jaouen F and Dodelet J P 2008 Controlled growth of Pt nanowires on carbon nanospheres and their enhanced performance as electrocatalysts in PEM fuel cells *Adv. Mater.* **20** 3900–4
- [6] An J, Kim Y-B, Park J, Gür T M and Prinz F B 2013 Three-dimensional nanostructured bilayer solid oxide fuel cell with 1.3 W/cm^2 at 450°C *Nano Lett.* **13** 4551–5
- [7] Fan Z, Razavi H, Do J-W, Moriwaki A, Ergen O, Chueh Y-L, Leu P W, Ho J C, Takahashi T and Reichertz L A 2009 Three-dimensional nanopillar-array photovoltaics on low-cost and flexible substrates *Nat. Mater.* **8** 648–53
- [8] Wang H-W, Ting C-F, Hung M-K, Chiou C-H, Liu Y-L, Liu Z, Ratnac K R and Ringer S P 2009 Three-dimensional electrodes for dye-sensitized solar cells: synthesis of indium-tin-oxide nanowire arrays and ITO/TiO₂ core-shell nanowire arrays by electrophoretic deposition *Nanotechnology* **20** 055601
- [9] Tétreault N, Arsenault É, Heiniger L-P, Soheilnia N, Brillet J, Moehl T, Zakeeruddin S, Ozin G A and Grätzel M 2011 High-efficiency dye-sensitized solar cell with three-dimensional photoanode *Nano Lett.* **11** 4579–84
- [10] Ha K, Jang E, Jang S, Lee J-K, Jang M S, Choi H, Cho J-S and Choi M 2016 A light-trapping strategy for nanocrystalline silicon thin-film solar cells using three-dimensionally assembled nanoparticle structures *Nanotechnology* **27** 055403
- [11] Jang S, Yoon J, Ha K, Kim M-C, Kim D H, Kim S M, Kang S M, Park S J, Jung H S and Choi M 2016 Facile fabrication of three-dimensional TiO₂ structures for highly efficient perovskite solar cells *Nano Energy* **22** 499–506
- [12] Leung S-F, Gu L, Zhang Q, Tsui K-H, Shieh J-M, Shen C-H, Hsiao T-H, Hsu C-H, Lu L and Li D 2014 Roll-to-roll fabrication of large scale and regular arrays of three-dimensional nanopikes for high efficiency and flexible photovoltaics *Sci. Rep.* **4** 4243
- [13] Soleymani L, Fang Z, Lam B, Bin X, Vasilyeva E, Ross A J, Sargent E H and Kelley S O 2011 Hierarchical nanotextured microelectrodes overcome the molecular transport barrier to achieve rapid, direct bacterial detection *ACS Nano* **5** 3360–6
- [14] Lee J H, Kim J S, Park J S, Lee W, Lee K E, Han S S, Lee K B and Lee J 2010 A three-dimensional and sensitive bioassay based on nanostructured quartz combined with viral nanoparticles *Adv. Funct. Mater.* **20** 2004–9
- [15] Zaumseil J, Meitl M A, Hsu J W, Acharya B R, Baldwin K W, Loo Y-L and Rogers J A 2003 Three-dimensional and multilayer nanostructures formed by nanotransfer printing *Nano Lett.* **3** 1223–7
- [16] Koops H W, Kretz J, Rudolph M and Weber M 1993 Constructive three-dimensional lithography with electron-beam induced deposition for quantum effect devices *J. Vac. Sci. Technol. B* **11** 2386–9
- [17] Jeon J, Floresca H C and Kim M 2010 Fabrication of complex three-dimensional nanostructures using focused ion beam and nanomanipulation *J. Vac. Sci. Technol. B* **28** 549–53
- [18] Matsui S 2007 Focused-ion-beam deposition for 3D nanostructure fabrication *Nucl. Instrum. Methods Phys. Res. B* **257** 758–64
- [19] Maruo S, Nakamura O and Kawata S 1997 Three-dimensional microfabrication with two-photon-absorbed photopolymerization *Opt. Lett.* **22** 132–4
- [20] Cumpston B H, Ananthavel S P, Barlow S, Dyer D L, Ehrlich J E, Erskine L L, Heikal A A, Kuebler S M, Lee I-Y S and McCord-Maughon D 1999 Two-photon polymerization initiators for three-dimensional optical data storage and microfabrication *Nature* **398** 51–4
- [21] Lee H, You S, Pikhitsa P V, Kim J, Kwon S, Woo C G and Choi M 2010 Three-dimensional assembly of nanoparticles from charged aerosols *Nano Lett.* **11** 119–24
- [22] Choi M, Lee H, You S and Woo C G 2008 *Array Formation of 3D Nanostructure of Nanoparticle via Electrodynamical Focusing of Charged Aerosols (Mt. Laurel, NJ, USA, October 2008)*
- [23] Kim H, Kim J, Yang H, Suh J, Kim T, Han B, Kim S, Kim D S, Pikhitsa P V and Choi M 2006 Parallel patterning of nanoparticles via electrodynamic focusing of charged aerosols *Nat. Nanotechnol.* **1** 117–21
- [24] You S, Han K, Kim H, Lee H, Woo C G, Jeong C, Nam W and Choi M 2010 High-resolution, parallel patterning of nanoparticles via an ion-induced focusing mask *Small* **6** 2146–52
- [25] Jung K et al 2014 Hotspot-engineered 3D multipetal flower assemblies for surface-enhanced Raman spectroscopy *Adv. Mater.* **26** 5924–9
- [26] Zheng X, Guo D, Shao Y, Jia S, Xu S, Zhao B and Xu W 2008 Photochemical modification of an optical fiber tip with a silver nanoparticle film: a SERS chemical sensor *Langmuir* **24** 4394–8
- [27] Vo-Dinh T, Wang H-N and Scaffidi J 2010 Plasmonic nanopores for SERS biosensing and bioimaging *J. Biophotonics* **3** 89–102
- [28] Lane L A, Qian X and Nie S 2015 SERS nanoparticles in medicine: from label-free detection to spectroscopic tagging *Chem. Rev.* **115** 10489–529
- [29] Han K, Kim W, Yu J, Lee J, Lee H, Woo C G and Choi M 2012 A study of pin-to-plate type spark discharge generator for producing unagglomerated nanoaerosols *J. Aerosol Sci.* **52** 80–8
- [30] Ha K, Choi H, Jung K, Han K, Lee J-K, Ahn K and Choi M 2014 Large-area assembly of three-dimensional nanoparticle structures via ion assisted aerosol lithography with a multipin spark discharge generator *Nanotechnology* **25** 225302
- [31] You S and Choi M 2007 Numerical simulation of microscopic motion and deposition of nanoparticles via electrodynamic focusing *J. Aerosol Sci.* **38** 1140–9
- [32] Joo T H, Kim M S and Kim K 1987 Surface-enhanced Raman scattering of benzenethiol in silver sol *J. Raman Spectrosc.* **18** 57–60